Atmospheric
Chemistry
and Physics
Discussions

Effects of *a priori* profile shape assumptions on comparisons between satellite NO₂ columns and model simulations

Matthew J. Cooper[1,2], Randall V. Martin[2,1,3], Daven K. Henze[4], Dylan B.A. Jones[5]

1. Department of Physics and Atmospheric Science, Dalhousie University, Halifax, Nova Scotia, Canada

2. Department of Energy, Environmental & Chemical Engineering, Washington University in St. Louis, St. Louis, Missouri, USA

3. Harvard-Smithsonian Center for Astrophysics, Cambridge, Massachusetts, USA

4. Department of Mechanical Engineering, University of Colorado, Boulder, Colorado, USA

5. Department of Physics, University of Toronto, Toronto, Ontario, Canada

Abstract

A critical step in satellite retrievals of trace gas columns is the calculation of the air mass factor (AMF) used to convert observed slant columns to vertical columns. This calculation requires *a priori* information on the shape of the vertical profile. As a result, comparisons between satellite-retrieved and model-simulated column abundances are influenced by the *a priori* profile shape. We examine how differences between the shape of the simulated and *a priori* profile can impact the interpretation of satellite retrievals by performing an adjoint-based 4D-Var assimilation of synthetic NO₂ observations for constraining NOₓ emissions. We use the GEOS-Chem Adjoint model to perform assimilations using a variety of AMFs to examine how *a posteriori* emission estimates are affected if the AMF is calculated using an *a priori* shape factor that is inconsistent with the simulated profile. In these tests, an inconsistent *a priori* shape factor increased errors in *a posteriori* emissions estimates by up to 80% over polluted regions. As the difference between the simulated profile shape and the *a priori* profile shape increases, so do the corresponding assimilated emission errors. This reveals the importance of using simulated profile information for AMF calculations when comparing that simulated output to satellite retrieved columns.

1. Introduction

Satellite observations provide a wealth of information on the abundance of trace gases in the troposphere (Fishman et al., 2008). The next generation of satellite instruments, including the upcoming geostationary constellation of TEMPO (Chance et al., 2013; Zoogman et al., 2017),

33   Sentinal-4 (Bazalgette Courrèges-Lacoste et al., 2011; Ingmann et al., 2012), and GEMS (Bak et

34   al., 2013; Kim, 2012), will provide information on NO_2 and other air quality relevant pollutants

35   on unprecedented spatial and temporal scales. Insight into processes that affect atmospheric

36   composition, including emissions (Streets et al., 2013), lifetimes (Fioletov et al., 2015; de Foy et

37   al., 2015; Laughner and Cohen, 2019), and deposition (Geddes and Martin, 2017; Kharol et al.,

38   2018) can be gained by interpreting this information with atmospheric chemistry models.

39   There are three main stages in retrieving trace gas abundances from ultraviolet and

40   visible solar backscatter radiance measurements: calculating a light-path "slant column" by

41   fitting observed spectra to known spectral signatures of trace gases, removing the stratospheric

42   portion of the column, and converting the slant column to a vertical column density using an air

43   mass factor (AMF). AMFs are calculated using a radiative transfer model and are a function of

44   viewing geometry, surface reflectance, clouds, and radiative transfer properties of the

45   atmosphere. AMF calculations also require an *a priori* estimate of the trace gas vertical profile

46   and are sensitive to the profile shape (Eskes and Boersma, 2003; Palmer et al., 2001).

47   Uncertainties in AMF calculations are the dominant source of uncertainty in satellite NO_2

48   retrievals over polluted regions (Boersma et al., 2007; Martin et al., 2002) largely due to

49   sensitivity to surface reflectance, clouds, aerosols, and *a priori* profile information (Lorente et

50   al., 2017).

51   Boersma et al. (2016) highlighted the issue of representativeness errors in comparing

52   model simulated values with UV-Vis satellite-retrieved columns. Vertical representativeness

53   errors arise from the satellite's altitude-dependent sensitivity due to atmospheric scattering and

54   can degrade the quality of model-measurement comparisons beyond errors that arise from either

55   modeling or measurements alone. A consistent accounting of the altitude-dependent sensitivity is

56   necessary to limit these errors.

57   Two common methods are used to account for vertical representativeness. In one method,

58   observed slant columns are converted to vertical columns using an air mass factor calculated

59   with scattering weights to represent instrument vertical sensitivity and shape factors to represent

60   the vertical profile (Palmer et al., 2001). Another commonly used method employs an AMF

61   provided with the retrieval to convert slant columns to vertical columns, and then applies an

62   averaging kernel to the simulated profile to resample the simulated profile in a manner that

63   mimics the satellite vertical sensitivity (Eskes and Boersma, 2003). In this method both the

64   averaging kernel and the retrieval AMF are calculated using an *a priori* NO$_2$ profile that may

65   have a different shape than the simulated profile, which may introduce errors in the observation-

66   simulation comparison (Zhu et al., 2016).

67   A common application of comparisons between satellite observed columns and model

68   simulations is to constrain NO$_x$ emissions (e.g. Ding et al., 2018; Ghude et al., 2013; Lamsal et

69   al., 2011; Martin et al., 2003; Vinken et al., 2014). One such approach is the use of four-

70   dimensional variational (4D-Var) data assimilation, which seeks to minimize a cost function that

71   accounts for the difference between simulated and retrieved values. As the cost function is a

72   difference between observed and simulated NO$_2$ columns, it is susceptible to vertical

73   representativeness errors resulting from inconsistent *a priori* vertical profile information. Studies

74   have shown that differences in retrieval processes between different NO$_2$ column products,

75   including differences in *a priori* profile shape, can propagate into errors of up to 50% in adjoint

76   inversions of NO$_x$ emissions (Qu et al., 2017). Studies have shown that shape factor errors can

77   impact emission estimates from other inversion methods as well (Laughner et al., 2016).

78   In this work we examine how *a priori* profile assumptions impact satellite-model

79   comparisons and use the GEOS-Chem adjoint as a case study to assess how this impact can

80   affect the interpretation of satellite observations. Section 2 provides the mathematical framework

81   for AMF calculations and satellite-model comparisons. Section 3 describes the adjoint model and

82   synthetic observations for the case study. Section 4 discusses the results.

83

84   **2. Mathematical frameworks**

85   **2.1 AMFs and averaging kernels**

86   The air mass factor translates the line-of-sight slant column abundances (Ω_s) retrieved

87   from satellite observed radiances into vertical column abundances (Ω_v). An air mass factor is the

88   ratio of Ω_s to Ω_v and depends on the atmospheric path as determined by geometry, NO$_2$ vertical

89   profile (***n***), surface reflectance, and radiative transfer properties of the atmosphere. Here we use

90   *M(**n**)* to represent an air mass factor derived using the vertical number density profile ***n***:

$$M(\boldsymbol{n}) = \frac{\Omega_s}{\Omega_v} \tag{1}$$

91

Atmospheric
Chemistry
and Physics
Discussions

92   In the method described by Palmer et al. (2001), a radiative transfer model is used calculate

93   scattering weights $w(z)$ (also known as box air mass factors) which characterize the sensitivity of

94   backscattered radiance I_B to the abundance of a trace gas at altitude z:

95

$$w(z) = -\frac{1}{M_g}\frac{\alpha_{a,z}}{\alpha_{eff}}\frac{\partial \ln{(I_B)}}{\partial \tau} \tag{2}$$

96   where $\alpha_{a,z}$ is the temperature-dependent absorption cross section (m^2 molec^{-1}), α_{eff} is the effective

97   (weighted average) absorption cross section (m^2 molec^{-1}) and $\partial \tau$ is the incremental trace gas

98   optical depth. M_G represents a geometric path correction accounting for the satellite viewing

99   geometry:

$$M_G = \sec \theta_o + \sec \theta \tag{3}$$

100   where θ is the solar zenith angle and θ_o is the satellite viewing angle. This information is then

101   combined with an *a priori* NO$_2$ shape factor (i.e. normalized vertical profile)

$$S(z) = \frac{n(z)}{\Omega_v} \tag{4}$$

102   typically calculated with an atmospheric chemistry model to provide an air mass factor via:

103

$$M(\boldsymbol{n}) = \int_0^{tropopause} \boldsymbol{w}(z)\boldsymbol{S}(z)dz \tag{5}$$

104   where $\boldsymbol{S(z)}$ is calculated using vertical profile $\boldsymbol{n(z)}$. An attribute of the formulation of Palmer et

105   al. (2001) is the independence of atmospheric radiative transfer properties $w(z)$ and the vertical

106   trace gas profile $S(z)$. The AMF definition in Equation (1) combined with Eq. (4) indicates that a

107   slant column can be calculated from a known vertical profile via:

$$\Omega_s = \int_0^{tropopause} \boldsymbol{w}(z)\boldsymbol{n}(z)dz \tag{6}$$

108

109   In an alternative formulation, the air mass factor is represented as part of an averaging

110   kernel. As formulated by Rodgers and Connor (2003), the averaging kernel ($\boldsymbol{A}$) provides the

111   information needed to relate the retrieved quantity $\boldsymbol{\hat{n}}$ to the true atmospheric profile $\boldsymbol{n}$:

112

$$\boldsymbol{\hat{n}} - \boldsymbol{n_a} = \boldsymbol{A}(\boldsymbol{n} - \boldsymbol{n_a}) \tag{7}$$

113   where $\boldsymbol{n_a}$ is an assumed *a priori* profile of number density. The elements of averaging kernel are

Atmospheric
Chemistry
and Physics
Discussions

114   related to the scattering weights by:

$$A(z) = \frac{w(z)}{M(n_a)} \tag{8}$$

115   where $M(n_a)$ is an air mass factor calculated using *a priori* vertical profile information. It is

116   important to note that unlike scattering weights, averaging kernels depend on the *a priori*

117   assumed vertical profile shape.

118   It is possible to decouple the radiative transfer information from the assumed vertical

119   profile information in an averaging kernel by converting the supplied averaging kernels to

120   scattering weights via:

$$w(z) = \frac{A(z)M(n_a)}{M_G} \tag{9}$$

121   A lexicon is given in Table 1 as notation used to describe these treatments has varied

122   across the literature. We choose M for air mass factor as a single letter is clearer in equations, w

123   for scattering weights to maintain the original formulation of Palmer et al. (2001), n for number

124   density following IUPAC recommendations, and Ω for column densities as is common in

125   radiative transfer literature.

126   Figure 1 shows examples of typical shape factor, scattering weight, and averaging kernel

127   profiles for a range of atmospheric conditions. NO_2 shape factors have significant variability;

128   Shape factors peak near the surface in urban regions due to local pollution sources, but peak in

129   the upper troposphere in more remote regions due to lightning. The shape of a scattering weight

130   profile depends strongly on surface reflectance and cloud conditions. Sensitivity in the lower

131   troposphere increases over reflective surfaces. Clouds increase sensitivity above due to their

132   reflectance but shield the satellite from observing the atmosphere below. Averaging kernels have

133   similarities with scattering weights but depend on both the shape of the prior and the satellite

134   sensitivity. As AMF calculations are a convolution of the shape factor and the scattering weight

135   profiles, these shapes affect NO_2 retrievals. For these examples, the AMF for a clear sky

136   observation with surface reflectance of 0.01 can range from 0.7 in an urban region to 1.7 in a

137   remote region. This large difference demonstrates the importance of the assumed profile shape to

138   the retrieval process.

139

140   **2.2 Comparing satellite observations to simulated values**

141

142 The following section expresses mathematically how satellite-model comparisons are made

143 using various *a priori* profiles.

144

2.2.1 Using scattering weights

146 Following Palmer et al. (2001), a retrieved vertical column ($\widehat{\Omega}_{v,o}$) is estimated using an

147 observed slant column $\Omega_{s,o}$ and a simulation-based air mass factor $M(\boldsymbol{n_m})$, which can be

148 calculated with Eq. (5) using the model-simulated NO_2 profile ($\boldsymbol{n_m}$):

149

$$\widehat{\Omega}_{v,o} = \frac{\Omega_{s,o}}{M(\boldsymbol{n_m})} \qquad (10)$$

150

151 The difference Δ_m between the estimated retrieved column and the model-simulated vertical

152 column ($\Omega_{v,m}$) is:

$$\Delta_m = \Omega_{v,m} - \widehat{\Omega}_{v,o} \qquad (11)$$

$$\Delta_m = \left(\sum_0^{tropopause} n_m \right) - \frac{\Omega_{s,o}}{M(\boldsymbol{n_m})} \qquad (12)$$

153 Equation (12) describes how this comparison is used in practice. However, we can rearrange this

154 expression in terms of model ($\Omega_{s,m}$) and observed ($\Omega_{s,o}$) slant columns using the definition of air

155 mass factor:

$$\Delta_m = \frac{\Omega_{s,m}}{M(\boldsymbol{n_m})} - \frac{\Omega_{s,o}}{M(\boldsymbol{n_m})} \qquad (13)$$

$$\Delta_m = \frac{1}{M(\boldsymbol{n_m})} \left(\Omega_{s,m} - \Omega_{s,o} \right) \qquad (14)$$

156

2.2.2 Using averaging kernels

158

159 Comparison of simulated and retrieved columns using the averaging kernel is described

160 by Eskes and Boersma (2003) and in the retrieval documentation in Boersma et al. (2011). The

161 averaging kernel is applied to the simulated profile in order to sample the simulated column in a

162 manner that reflects the retrieval sensitivity:

$$\widehat{\Omega}_{v,m} = \sum_0^{tropopause} A\boldsymbol{n_m} \qquad (15)$$

163   The resampled simulated column is then compared to the retrieved vertical column ($\Omega_{v,o}$) using

164   the *a priori*-based air mass factor $M(n_a)$ supplied with the retrieval dataset:

165

$$\Delta_a = \widehat{\Omega}_{v,m} - \Omega_{v,o} \tag{16}$$

$$\Delta_a = \sum_0^{tropopause} An_m - \frac{\Omega_{s,o}}{M(n_a)} \tag{17}$$

166   Equation (17) describes how this method is used in practice. To facilitate the comparison with

167   Eq. (14), Eq. (17) can be rewritten using an alternative formulation relating averaging kernels to

168   scattering weights:

169

$$\Delta_a = \sum_0^{tropopause} \frac{wn_m}{M(n_a)} - \frac{\Omega_{s,o}}{M(n_a)} \tag{18}$$

$$\Delta_a = \frac{1}{M(n_a)}\left(\Omega_{s,m} - \Omega_{s,o}\right) \tag{19}$$

170

171   By comparing Eq. (14) to Eq. (19), it is evident that the underlying difference between the two

172   approaches is the choice of *a priori* profile information used to calculate the AMF, as the

173   averaging kernel method is not independent of *a priori* profile assumptions. This bias could be

174   addressed by replacing the *a priori* -based AMF in Eq. (18) with a simulation-based AMF using

175   the following relationship (Boersma et al., 2016; Lamsal et al., 2010):

$$M(n_m) = M(n_a)\frac{\sum An_a}{\sum n_m} \tag{20}$$

176   It should be noted that both the averaging kernel and scattering weight methods are

177   equivalent for comparisons that examine ratios of retrieved and modeled columns:

$$r_m = \frac{\widehat{\Omega_{v,o}}}{\Omega_{v,m}} = \frac{\Omega_{s,o}/M(n_m)}{\sum n_m} = \frac{\Omega_{s,o}}{\sum n_m}\frac{\sum n_m}{\sum wn_m} = \frac{\Omega_{s,o}}{\sum wn_m} \tag{21}$$

$$r_a = \frac{\Omega_{v,o}}{\widehat{\Omega_{v,m}}} = \frac{\Omega_{s,o}/M(n_a)}{\sum An_m} = \frac{\Omega_{s,o}/M(n_a)}{\sum wn_m/M(n_a)} = \frac{\Omega_{s,o}}{\sum wn_m} \tag{22}$$

178

179   For ratios, both methods are dependent on geophysical assumptions used to calculate scattering

180   weights but are independent of *a priori* profile information.

181

3. Tools and Methodology

3.1 GEOS-Chem and its adjoint

182

183

184   The GEOS-Chem chemical transport model (www.geos-chem.org) is used to create

185 synthetic NO_2 observations and for their analysis. The GEOS-Chem version used here is version

186 35j of the GEOS-Chem Adjoint model. GEOS-Chem includes a detailed oxidant-aerosol

187 chemical mechanism (Bey et al., 2001; Park et al., 2004) and uses assimilated meteorological

188 fields from the Goddard Earth Observation System (GEOS-5), with 47 vertical levels up to 0.01

189 hPa and a horizontal resolution of 4°x5°. Global anthropogenic NO_x emissions are provided by

190 the Emission Database for Global Atmospheric Research (EDGAR) inventory (Olivier et al.,

191 2005) with regional overwrites over North America (EPA/NEI99), Europe (EMEP), Canada

192 (CAC), Mexico (BRAVO, (Kuhns et al., 2005)), and East Asia (Streets et al., 2006). Other NO_x

193 sources include biomass burning (GFED2 (Van der Werf et al., 2010)), lightning (Murray et al.,

194 2012), and soils (Wang et al., 1998). This model has been used previously to constrain NO_x

195 emissions (Cooper et al., 2017; Henze et al., 2009; Qu et al., 2017, 2019; Xu et al., 2013; Zhang

196 et al., 2016).

197   The GEOS-Chem adjoint (Henze et al., 2007, 2009) is used here to perform a 4D-Var

198 data assimilation. The adjoint seeks to iteratively minimize a cost function generally defined by

199 the difference between satellite retrieved and simulated columns (Δ, from either Eq. (12) or Eq.

200 (17)):

$$J = \frac{1}{2}\Delta^T S_o^{-1} \Delta + \frac{1}{2}\gamma_R (E - E_a)^T S_E^{-1}(E - E_a) \tag{22}$$

201 where E and E_a are the *a posteriori* and *a priori* emissions, S_o and S_E are the retrieval and *a*

202 *priori* emission error covariance matrices, and γ_R is a regularization parameter that allows for

203 weighting the cost function towards the retrieved columns or *a priori* emissions.

204

3.2 Experiment Outline

205

206   In this study we perform 4D-Var data assimilation experiments to infer surface NO_x

207 emissions using synthetic NO_2 observations. We use synthetic observations built from a known

208 emission inventory to provide a "truth" that can be used to evaluate the inversion results. To

209 demonstrate how *a priori* profile information can propagate in an assimilation, we use either the

210   model profile (Δ_m, Eq. (12)) or an *a priori* profile (Δ_a, Eq. (17)) in the cost function. For these

211   tests, we use one observation per hour per 4°x5° grid box for a period of two weeks in July 2010.

212   A one-week spin-up window at the start of each adjoint iteration is used to allow NO_x to reach

213   steady state. Observation error covariances S_o are described as a relative error of 30% of the slant

214   column density, plus an absolute error of 10^{15} molecules cm^{-2}, which is representative of typical

215   satellite retrieved NO_2 column uncertainties (Boersma et al., 2007; Martin et al., 2002). We omit

216   the *a priori* emissions constraint in the cost function (i.e. set $\gamma_R=0$) to isolate the impact of the

217   observations.

218

219   **3.2.1 Synthetic observations**

220   Synthetic observations are created using a GEOS-Chem simulation where random

221   Gaussian noise with a standard deviation of 5% is added to the anthropogenic NO_x emissions. No

222   additional noise is added to the individual observations to isolate the impact of AMF errors

223   against- additional sources of uncertainty. Figure 2 shows the standard (*a priori*) anthropogenic

224   NO_x emissions and the changes used to create the "true" emissions for the synthetic

225   observations.

226   Observations consist of synthetic slant columns ($\Omega_{s,o}$) created by applying scattering

227   weights to the synthetic vertical profiles using Eq. (6). To represent typical conditions, average

228   scattering weight profiles for each grid box are found by averaging scattering weights for OMI

229   observations during July 2010. OMI scattering weights are calculated using the LIDORT

230   radiative transfer model (Spurr, 2002) by providing LIDORT with the observation geometry of

231   the OMI observations and aerosol profiles from the GEOS-Chem base simulation.

232

233   **3.2.2 Shape Factors**

234   To test the impact of *a priori* profile information, five different tests are performed using

235   five different NO_2 profile shapes for AMF calculations:

236   •   Case SF_M : The GEOS-Chem model simulated profile (n_m), updated at each iteration

237   of the adjoint run

238   •   Case SF_{prior}: The *a priori* GEOS-Chem simulated profile, without updating.

239   •   Case SF_{n30}: An *a priori* profile created by a GEOS-Chem simulation where global

240   anthropogenic NO_x emissions were perturbed with random Gaussian noise with a

241   standard deviation of 30%. In cases where this results in negative emissions, a value

242   of zero is used.

243   • Case SF_{trop}: An *a priori* profile that assumes the NO_2 profile shape is uniform from

244   the surface to the tropopause (~200 hPa).

245   • Case SF_{BL}: An *a priori* profile that assumes the NO_2 profile shape is uniform from the

246   surface to the boundary layer (~800 hPa).

247

248   An advantage of using scattering weights and the simulated shape factor in a 4D-Var framework

249   is that it allows for the shape factor, and thus the AMF, to be updated at each iteration. When *a*

250   *priori* profiles from an external source are used it is not possible for them to update during the

251   inversion. The SF_M and SF_{prior} cases will test the impact that iterative updates to the AMF will

252   have on *a posteriori* estimates. The additional cases will test for the impact of using an averaging

253   kernel based on *a priori* profile assumptions that are inconsistent with the model. In practice,

254   averaging kernels and *a priori* profiles included in retrieval data sets are generally derived from

255   chemical transport models that have different physical processes, emissions, or spatial

256   resolutions. The SF_{n30} test is representative of an inversion that uses *a priori* profile information

257   from a different chemical transport model with similar resolution but different emissions. The

258   SF_{BL} and SF_{trop} tests are extreme examples of using an *a priori* based on a coarser resolution

259   model, as both tests assume no spatial variability. The SF_{BL} profile is representative of polluted

260   regions as indicated by the typical urban profile in Fig. 1, while the SF_{trop} profile is

261   representative of a typical rural profile.

262

263   **4. Results**

264   Figure 3 shows root mean square errors (RMSE) for the *a posteriori* emissions estimated

265   by the 4D-Var assimilation tests. All tests successfully reduce the *a priori* emission error by an

266   order of magnitude or more. The SF_M has the lowest RMSE indicating that it can best estimate

267   the "true" emissions. The next lowest RMSE is for the SF_{prior} test, which uses the same initial

268   model shape factor but does not update during the adjoint iterations, followed by the SF_{n30},

269   SF_{trop}, and SF_{BL} tests.

270   Figure 4 shows maps of the difference in RMSE between the SF_M test and the other tests.

271   The SF_M test has a lower RMSE than the other tests in 65-72% grid boxes where the difference is

272   nonzero. Again, the SF_{prior} test is closest to the SF_M test with a mean absolute difference of 6×10^6

273   molec/cm^2/s, followed by SF_{n30} (7×10^6 molec/cm^2/s), SF_{trop}, (13×10^6 molec/cm^2/s), and SF_{BL}

274   (16×10^6 molec/cm^2/s).

275   Table 2 summarizes additional error statistics focused on grid boxes with significant

276   emission sources. Errors in *a posteriori* emission estimates are correlated with the "true"

277   emissions in the SF_{trop} and SF_{n30} tests, indicating that these tests are not well constraining the

278   emissions. Differences between tests are more significant over polluted regions where AMF

279   errors are more influential; For example, in the regions with the highest NO$_x$ emissions, RMSE

280   values indicate SF_M outperforms SF_{n30} by 30% and SF_{trop} by >80%. Another sign of adjoint

281   inversion quality is a low variance in errors. While the posterior error is reduced relative to the *a*

282   *priori* error in all tests, error standard deviations are 30% higher for SF_{n30} and 90% higher for

283   SF_{trop} compared to SFM. The global maximum error for the SFtrop test is 30% higher than the

284   SF_M test. All metrics indicate that the SF_M test best represents the "true" emissions.

285

286   **5. Discussion**

287   Accounting for the vertical profile dependence of satellite observations is essential to

288   accurately interpret those observations. This work examines how the choice of shape factor

289   affects differences between simulated and satellite-retrieved quantities in a 4D-Var assimilation

290   framework. Examination of the mathematical frameworks behind two common methods for

291   comparing simulated and retrieved columns highlights how the method introduced by Palmer et

292   al. (2001) facilitates separation of observation sensitivity (scattering weights) from the profile

293   shape (shape factor) enabling the model-retrieval comparison to be independent of *a priori*

294   profile assumptions.

295   In these case studies, vertical representativeness errors were best reduced by using a

296   shape factor that was consistent with the model simulation. This was especially true in polluted

297   regions where the AMF errors dominate observation uncertainties, as deviations between the

298   tests were largest in these regions. The further the shape factor deviated from the model state the

299   larger the inversion errors became, as indicated by Fig. 5. Comparing the SF_M and SF_{prior} tests

300   shows that allowing for shape factor to update during the iterative adjoint process further reduces

301   the RMSE by 10%. However, even without allowing for shape factor updates, using a shape

302   factor that is consistent with the model state produces a more accurate inversion result than using

303   other assumed profile shapes.

304   The case study presented here demonstrates that the shape factor source can have a strong

305   influence on adjoint inversion results. However, the magnitude of this influence can vary.

306   Additional tests performed using synthetic observations built using random 15% or 30%

307   perturbations to emissions (rather than the 5% perturbation used here) were insensitive to the

308   AMF. In these tests, the adjoint cost function was more sensitive to the larger difference between

309   the observed and simulated slant columns (i.e. Ω_m - Ω_o in Eq. (13) and (18)) than to AMF. This

310   indicates that the adjoint inversion is less sensitive to vertical representativeness errors in cases

311   where emissions are poorly constrained; Conversely, choice of AMF will become increasingly

312   important to adjoint inversions as emission inventories improve. Furthermore, omitting the *a*

313   *priori* emissions constraint in the cost function and omitting noise in the observations in these

314   tests to isolate the impact of the AMF effectively assumes poorly constrained *a priori* emissions

315   and ideal observations. In practice, cost function sensitivity to AMF choice may be buffered

316   when *a priori* emissions uncertainties and observational noise are considered.

317   As it is beneficial for a consistent shape factor to be used when comparing satellite

318   retrieved values to model simulated results, it will be useful for data products to provide the

319   information required for this method to the user community. This is most straightforward when

320   scattering weights (rather than averaging kernels) are provided alongside retrieved column data,

321   as scattering weights and shape factors are independently calculated, however averaging kernels

322   can be converted to scattering weights if the *a priori* profiles used are included in the dataset.

323   In summary, when comparing a model simulation to a satellite retrieved NO_2 column in a

324   4D-Var environment, calculating the AMF using the simulated shape factor allows for better

325   accuracy in inversion results. This demonstration can provide general guidance for other

326   methods of interpreting satellite observations with models, as using the simulated shape factor

327   assures consistency in the vertical representativeness between model and retrieval.

328

329   7. Author Contributions

330   MC designed and carried out the case studies and their analysis. All co-authors provided

331   guidance in analyzing results. MC prepared the manuscript with contributions from all co-

332   authors.

333

Atmospheric
Chemistry
and Physics
Discussions

334 **8. Competing interests**

335 The authors declare that they have no conflict of interest.

336

337 **9. Acknowledgements**

340

341 **10. Data Availability**

342 The GEOS-Chem chemical transport model and its adjoint are available at www.geos-chem.org
343 (last access: 20 August 2017). OMI NO_2 data used in this study is available from the NASA
344 Goddard Earth Sciences Data and Information Services Center (https://disc.sci.gsfc.nasa.gov;
345 last access: 14 March 2019). AMF code (Spurr, 2002; Martin et al., 2002) used to calculate
346 scattering weights and air mass factors is available at http://fizz.phys.dal.ca/~atmos (last access:
347 19 June 2017).

348

349 **11. References**

350 Bak, J., Kim, J. H., Liu, X., Chance, K. and Kim, J.: Geoscientific Instrumentation Methods and

351 Data Systems Evaluation of ozone profile and tropospheric ozone retrievals from GEMS and

352 OMI spectra, Atmos. Meas. Tech, 6, 239–249, doi:10.5194/amt-6-239-2013, 2013.

353 Bazalgette Courrèges-Lacoste, G., Ahlers, B., Guldimann, B., Short, A., Veihelmann, B. and

354 Stark, H.: The Sentinel-4/UVN instrument on-board MTG-S, in EUMETSAT Meteorological

355 Satellite Conference, Oslo, Norway., 2011.

356 Bey, I., Jacob, D. J., Yantosca, R. M., Logan, J. A., Field, B. D., Fiore, A. M., Li, Q., Liu, H. Y.,

357 Mickley, L. J. and Schultz, M. G.: Global modeling of tropospheric chemistry with assimilated

358 meteorology: Model description and evaluation, J. Geophys. Res. Atmos., 106(D19), 23073–

359 23095, 2001.

360 Boersma, K., Braak, R. and van der A, R. J.: Dutch OMI NO2 (DOMINO) data product v2. 0,

361 Tropospheric Emissions Monitoring Internet Service on-line documentation, [online] Available

362 from: http://www.temis.nl/docs/OMI_NO2_HE5_2.0_2011.pdf, 2011.

363 Boersma, K. F., Eskes, H. J., Veefkind, J. P., Brinksma, E. J., van der A, R. J., Sneep, M., van

364 den Oord, G. H. J., Levelt, P. F., Stammes, P., Gleason, J. F. and Bucsela, E. J.: Near-real time

365 retrieval of tropospheric NO2 from OMI, Atmos. Chem. Phys., 7(8), 2103–2118,

366 doi:10.5194/acp-7-2103-2007, 2007.

Atmospheric
Chemistry
and Physics
Discussions
Open Access
EGU

367 Boersma, K. F., Vinken, G. C. M. and Eskes, H. J.: Representativeness errors in comparing

368 chemistry transport and chemistry climate models with satellite UV–Vis tropospheric column

369 retrievals, Geosci. Model Dev, 9, 875–898, doi:10.5194/gmd-9-875-2016, 2016.

370 Chance, K., Liu, X., Suleiman, R. M., Flittner, D. E., Al-Saadi, J. and Janz, S. J.: Tropospheric

371 emissions: monitoring of pollution (TEMPO), edited by J. J. Butler, X. (Jack) Xiong, and X. Gu,

372 p. 88660D, International Society for Optics and Photonics., 2013.

373 Cooper, M., Martin, R. V., Padmanabhan, A. and Henze, D. K.: Comparing mass balance and

374 adjoint methods for inverse modeling of nitrogen dioxide columns for global nitrogen oxide

375 emissions, J. Geophys. Res. Atmos., doi:10.1002/2016JD025985, 2017.

376 Ding, J., van der A, R. J., Mijling, B., Jalkanen, J.-P., Johansson, L. and Levelt, P. F.: Maritime

377 NOx Emissions Over Chinese Seas Derived From Satellite Observations, Geophys. Res. Lett.,

378 45(4), 2031–2037, doi:10.1002/2017GL076788, 2018.

379 Eskes, H. J. and Boersma, K. F.: Averaging kernels for DOAS total-column satellite retrievals,

380 Atmos. Chem. Phys., 3(5), 1285–1291, 2003.

381 Fioletov, V. E., McLinden, C. A., Krotkov, N. and Li, C.: Lifetimes and emissions of SO2 from

382 point sources estimated from OMI, Geophys. Res. Lett., 42(6), 1969–1976,

383 doi:10.1002/2015GL063148, 2015.

384 Fishman, J., Al-Saadi, J. A., Creilson, J. K., Bowman, K. W., Burrows, J. P., Richter, A.,

385 Chance, K. V., Edwards, D. P., Martin, R. V., Morris, G. A., Pierce, R. B., Ziemke, J. R.,

386 Schaack, T. K., Thompson, A. M., Fishman, J., Al-Saadi, J. A., Creilson, J. K., Bowman, K. W.,

387 Burrows, J. P., Richter, A., Chance, K. V., Edwards, D. P., Martin, R. V., Morris, G. A., Pierce,

388 R. B., Ziemke, J. R., Schaack, T. K. and Thompson, A. M.: Remote Sensing of Tropospheric

389 Pollution from Space, Bull. Am. Meteorol. Soc., 89(6), 805–821,

390 doi:10.1175/2008BAMS2526.1, 2008.

391 de Foy, B., Lu, Z., Streets, D. G., Lamsal, L. N. and Duncan, B. N.: Estimates of power plant NO

392 x emissions and lifetimes from OMI NO 2 satellite retrievals, Atmos. Environ., 116, 1–11, 2015.

393 Geddes, J. A. and Martin, R. V.: Global deposition of total reactive nitrogen oxides from 1996 to

394 2014 constrained with satellite observations of NO2 columns, Atmos. Chem. Phys., 17(16),

395 10071–10091, doi:10.5194/acp-17-10071-2017, 2017.

396 Ghude, S. D., Pfister, G. G., Jena, C., van der A, R. J., Emmons, L. K. and Kumar, R.: Satellite

397 constraints of nitrogen oxide (NOx) emissions from India based on OMI observations and WRF-

398   Chem simulations, Geophys. Res. Lett., 40(2), 423–428, 2013.

399   Henze, D. K., Hakami, A. and Seinfeld, J. H.: Development of the adjoint of GEOS-Chem,

400   Atmos. Chem. Phys., 7(9), 2413–2433, doi:10.5194/acp-7-2413-2007, 2007.

401   Henze, D. K., Seinfeld, J. H. and Shindell, D. T.: Inverse modeling and mapping US air quality

402   influences of inorganic PM 2.5 precursor emissions using the adjoint of GEOS-Chem, Atmos.

403   Chem. Phys., 9(16), 5877–5903, 2009.

404   Ingmann, P., Veihelmann, B., Langen, J., Lamarre, D., Stark, H. and Courrèges-Lacoste, G. B.:

405   Requirements for the GMES Atmosphere Service and ESA's implementation concept: Sentinels-

406   4/-5 and -5p, Remote Sens. Environ., 120, 58–69, doi:10.1016/j.rse.2012.01.023, 2012.

407   Kharol, S. K., Shephard, M. W., McLinden, C. A., Zhang, L., Sioris, C. E., O'Brien, J. M., Vet,

408   R., Cady-Pereira, K. E., Hare, E., Siemons, J. and Krotkov, N. A.: Dry Deposition of Reactive

409   Nitrogen From Satellite Observations of Ammonia and Nitrogen Dioxide Over North America,

410   Geophys. Res. Lett., 45(2), 1157–1166, doi:10.1002/2017GL075832, 2018.

411   Kim, J.: GEMS (Geostationary Environment Monitoring Spectrometer) onboard the

412   GeoKOMPSAT to monitor air quality in high temporal and spatial resolution over Asia-Pacific

413   Region, in EGU General Assembly Conference Abstracts, vol. 14, p. 4051., 2012.

414   Kuhns, H., Knipping, E. M. and Vukovich, J. M.: Development of a United States–Mexico

415   emissions inventory for the big bend regional aerosol and visibility observational (BRAVO)

416   study, J. Air Waste Manage. Assoc., 55(5), 677–692, 2005.

417   Lamsal, L. N., Martin, R. V., Van Donkelaar, A., Celarier, E. A., Bucsela, E. J., Boersma, K. F.,

418   Dirksen, R., Luo, C. and Wang, Y.: Indirect validation of tropospheric nitrogen dioxide retrieved

419   from the OMI satellite instrument: Insight into the seasonal variation of nitrogen oxides at

420   northern midlatitudes, J. Geophys. Res. Atmos., doi:10.1029/2009JD013351, 2010.

421   Lamsal, L. N., Martin, R. V, Padmanabhan, A., van Donkelaar, A., Zhang, Q., Sioris, C. E.,

422   Chance, K., Kurosu, T. P. and Newchurch, M. J.: Application of satellite observations for timely

423   updates to global anthropogenic NOx emission inventories, Geophys. Res. Lett., 38(5), 2011.

424   Laughner, J. L. and Cohen, R. C.: Direct observation of changing NOx lifetime in North

425   American cities, Science (80-.)., 366(6466), 723–727, doi:10.1126/science.aax6832, 2019.

426   Laughner, J. L., Zare, A. and Cohen, R. C.: Effects of daily meteorology on the interpretation of

427   space-based remote sensing of NO 2, Atmos. Chem. Phys, 16, 15247–15264, doi:10.5194/acp-

428   16-15247-2016, 2016.

429   Lorente, A., Folkert Boersma, K., Yu, H., Dörner, S., Hilboll, A., Richter, A., Liu, M., Lamsal,

430   L. N., Barkley, M., De Smedt, I., Van Roozendael, M., Wang, Y., Wagner, T., Beirle, S., Lin, J.-

431   T., Krotkov, N., Stammes, P., Wang, P., Eskes, H. J. and Krol, M.: Structural uncertainty in air

432   mass factor calculation for NO2 and HCHO satellite retrievals, Atmos. Meas. Tech., 10(3), 759–

433   782, doi:10.5194/amt-10-759-2017, 2017.

434   Martin, R. V., Jacob, D. J., Chance, K., Kurosu, T. P., Palmer, P. I. and Evans, M. J.: Global

435   inventory of nitrogen oxide emissions constrained by space-based observations of NO2 columns,

436   J. Geophys. Res., 108(D17), 4537, doi:10.1029/2003JD003453, 2003.

437   Martin, R. V, Chance, K., Jacob, D. J., Kurosu, T. P., Spurr, R. J. D., Bucsela, E., Gleason, J. F.,

438   Palmer, P. I., Bey, I. and Fiore, A. M.: An improved retrieval of tropospheric nitrogen dioxide

439   from GOME, J. Geophys. Res. Atmos., 107(D20), 4437, doi:10.1029/2001JD001027, 2002a.

440   Martin, R. V, Jacob, D. J., Logan, J. A., Bey, I., Yantosca, R. M., Staudt, A. C., Li, Q., Fiore, A.

441   M., Duncan, B. N. and Liu, H.: Interpretation of TOMS observations of tropical tropospheric

442   ozone with a global model and in situ observations, J. Geophys. Res. Atmos., 107(D18), 2002b.

443   Murray, L. T., Jacob, D. J., Logan, J. A., Hudman, R. C. and Koshak, W. J.: Optimized regional

444   and interannual variability of lightning in a global chemical transport model constrained by

445   LIS/OTD satellite data, J. Geophys. Res. Atmos., 117(D20), 2012.

446   Olivier, J. G. J., Van Aardenne, J. A., Dentener, F. J., Pagliari, V., Ganzeveld, L. N. and Peters,

447   J. A. H. W.: Recent trends in global greenhouse gas emissions: regional trends 1970–2000 and

448   spatial distributionof key sources in 2000, Environ. Sci., 2(2–3), 81–99, 2005.

449   Palmer, P. I., Jacob, D. J., Chance, K. and Martin, R. V: Air mass factor formulation for

450   spectroscopic measurements from satellites' Application to formaldehyde retrievals from the

451   Global Ozone Monitoring Experiment, J. Geophys. Res., 106(D13), 14,539-14550,

452   doi:10.1029/2000JD900772, 2001.

453   Park, R. J., Jacob, D. J., Field, B. D., Yantosca, R. M. and Chin, M.: Natural and transboundary

454   pollution influences on sulfate-nitrate-ammonium aerosols in the United States: Implications for

455   policy, J. Geophys. Res. Atmos., 109(D15), 2004.

456   Qu, Z., Henze, D. K., Capps, S. L., Wang, Y., Xu, X., Wang, J. and Keller, M.: Monthly top-

457   down NOx emissions for China (2005-2012): A hybrid inversion method and trend analysis, J.

458   Geophys. Res. Atmos., doi:10.1002/2016JD025852, 2017.

459   Qu, Z., Henze, D. K., Theys, N., Wang, J. and Wang, W.: Hybrid mass balance/4D-Var joint

460   inversion of NOx and SO2 emissions in East Asia, J. Geophys. Res. Atmos., 2018JD030240,

461   doi:10.1029/2018JD030240, 2019.

462   Rodgers, C. D. and Connor, B. J.: Intercomparison of remote sounding instruments, J. Geophys.

463   Res. Atmos., 108(D3), 2003.

464   Spurr, R. J. D.: Simultaneous derivation of intensities and weighting functions in a general

465   pseudo-spherical discrete ordinate radiative transfer treatment, J. Quant. Spectrosc. Radiat.

466   Transf., 75(2), 129–175, doi:10.1016/S0022-4073(01)00245-X, 2002.

467   Streets, D. G., Zhang, Q., Wang, L., He, K., Hao, J., Wu, Y., Tang, Y. and Carmichael, G. R.:

468   Revisiting China's CO emissions after the transport and chemical evolution over the Pacific

469   (TRACE-P) mission: synthesis of inventories, atmospheric modeling, and observations, J.

470   Geophys. Res. Atmos., 111(D14), 2006.

471   Streets, D. G., Canty, T., Carmichael, G. R., De Foy, B., Dickerson, R. R., Duncan, B. N.,

472   Edwards, D. P., Haynes, J. A., Henze, D. K., Houyoux, M. R., Jacob, D. J., Krotkov, N. A.,

473   Lamsal, L. N., Liu, Y., Lu, Z., Martin, R. V., Pfister, G. G., Pinder, R. W., Salawitch, R. J. and

474   Wecht, K. J.: Emissions estimation from satellite retrievals: A review of current capability,

475   Atmos. Environ., 77, 1011–1042, doi:10.1016/j.atmosenv.2013.05.051, 2013.

476   Vinken, G. C. M., Boersma, K. F., Maasakkers, J. D., Adon, M. and Martin, R. V.: Worldwide

477   biogenic soil NOx emissions inferred from OMI NO2 observations, Atmos. Chem. Phys.,

478   doi:10.5194/acp-14-10363-2014, 2014.

479   Wang, Y., Jacob, D. J. and Logan, J. A.: Global simulation of tropospheric O3-NO x-

480   hydrocarbon chemistry: 1. Model formulation, J. Geophys. Res. Atmos., 103(D9), 10713–10725,

481   1998.

482   Van der Werf, G. R., Randerson, J. T., Giglio, L., Collatz, G. J., Mu, M., Kasibhatla, P. S.,

483   Morton, D. C., DeFries, R. S., Jin, Y. van and van Leeuwen, T. T.: Global fire emissions and the

484   contribution of deforestation, savanna, forest, agricultural, and peat fires (1997–2009), Atmos.

485   Chem. Phys., 10(23), 11707–11735, 2010.

486   Xu, X., Wang, J., Henze, D. K., Qu, W. and Kopacz, M.: Constraints on aerosol sources using

487   GEOS-Chem adjoint and MODIS radiances, and evaluation with multisensor (OMI, MISR) data,

488   J. Geophys. Res. Atmos., 118(12), 6396–6413, doi:10.1002/jgrd.50515, 2013.

489   Zhang, L., Shao, J., Lu, X., Zhao, Y., Hu, Y., Henze, D. K., Liao, H., Gong, S. and Zhang, Q.:

490   Sources and Processes Affecting Fine Particulate Matter Pollution over North China: An Adjoint

491   Analysis of the Beijing APEC Period, Environ. Sci. Technol., 50(16), 8731–8740,

492   doi:10.1021/acs.est.6b03010, 2016.

493   Zhu, L., Jacob, D. J., Kim, P. S., Fisher, J. A., Yu, K., Travis, K. R., Mickley, L. J., Yantosca, R.

494   M., Sulprizio, M. P., De Smedt, I., González Abad, G., Chance, K., Li, C., Ferrare, R., Fried, A.,

495   Hair, J. W., Hanisco, T. F., Richter, D., Jo Scarino, A., Walega, J., Weibring, P. and Wolfe, G.

496   M.: Observing atmospheric formaldehyde (HCHO) from space: validation and intercomparison

497   of six retrievals from four satellites (OMI, GOME2A, GOME2B, OMPS) with SEAC4RS

498   aircraft observations over the southeast US, Atmos. Chem. Phys., 16(21), 13477–13490,

499   doi:10.5194/acp-16-13477-2016, 2016.

500   Zoogman, P., Liu, X., Suleiman, R. M., Pennington, W. F., Flittner, D. E., Al-Saadi, J. A.,

501   Hilton, B. B., Nicks, D. K., Newchurch, M. J., Carr, J. L., Janz, S. J., Andraschko, M. R., Arola,

502   A., Baker, B. D., Canova, B. P., Chan Miller, C., Cohen, R. C., Davis, J. E., Dussault, M. E.,

503   Edwards, D. P., Fishman, J., Ghulam, A., González Abad, G., Grutter, M., Herman, J. R., Houck,

504   J., Jacob, D. J., Joiner, J., Kerridge, B. J., Kim, J., Krotkov, N. A., Lamsal, L., Li, C., Lindfors,

505   A., Martin, R. V., McElroy, C. T., McLinden, C., Natraj, V., Neil, D. O., Nowlan, C. R.,

506   O'Sullivan, E. J., Palmer, P. I., Pierce, R. B., Pippin, M. R., Saiz-Lopez, A., Spurr, R. J. D.,

507   Szykman, J. J., Torres, O., Veefkind, J. P., Veihelmann, B., Wang, H., Wang, J. and Chance, K.:

508   Tropospheric emissions: Monitoring of pollution (TEMPO), J. Quant. Spectrosc. Radiat. Transf.,

509   186, 17–39, doi:10.1016/j.jqsrt.2016.05.008, 2017.

510

511

512   Figures:

513

514
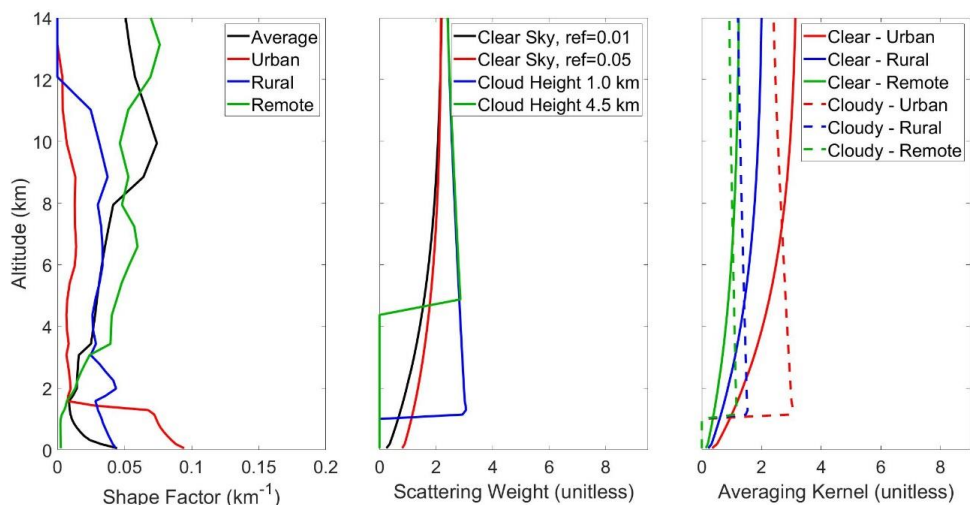
Figure 1: (Left) Shape factor profiles from a GEOS-Chem simulation for July 2010. Shown are a global average, and typical urban (Beijing), rural (Midwest USA), and remote (Tropical Pacific) profiles. (Middle) Typical OMI scattering weight profiles for varying surface reflectance and cloud height. (Right) Averaging kernels calculated using the same shape factors and scattering weights ("Clear Sky" surface reflectance is 0.01, "Cloudy" uses cloud height of 1 km).
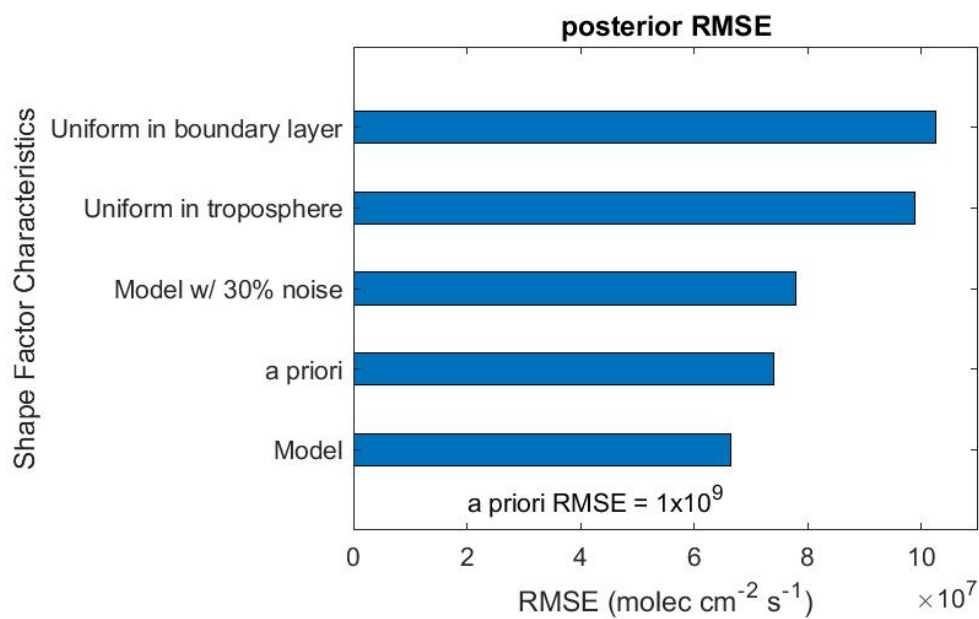
520
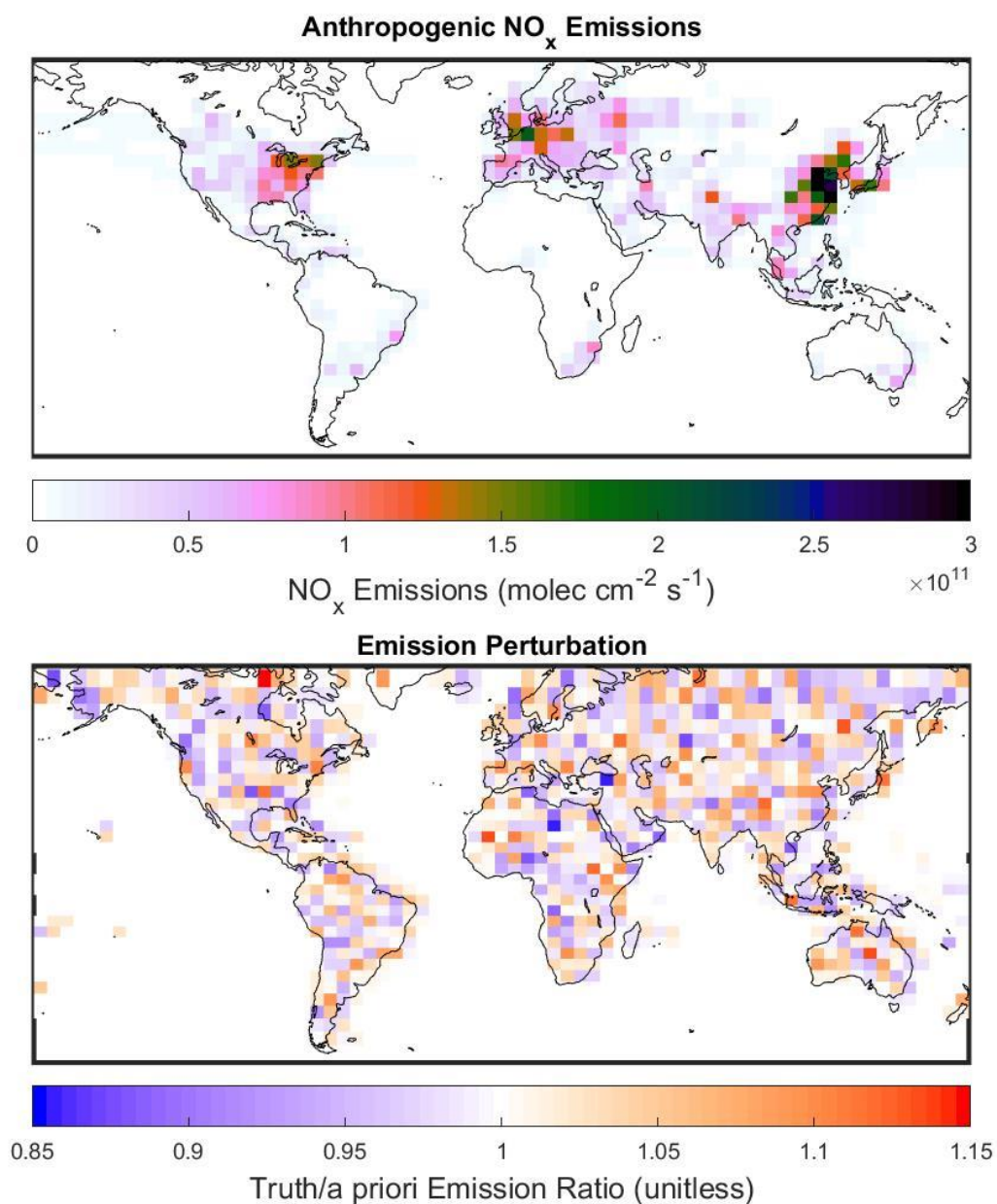
521
522 Figure 2 (top) Anthropogenic NO$_x$ emissions for July 2010 used in GEOS-Chem. (bottom) Ratio
523 of "true" emissions used to create synthetic observations to a priori NO$_x$ emissions.
524

Atmospheric
Chemistry
and Physics
Discussions

525
Figure 3: Global root mean square error (RMSE) values for 4D-Var estimates of NO_x emissions
527   for tests using various shape factors in AMF calculations.
528

Atmospheric
Chemistry
and Physics
Discussions

Open Access

EGU
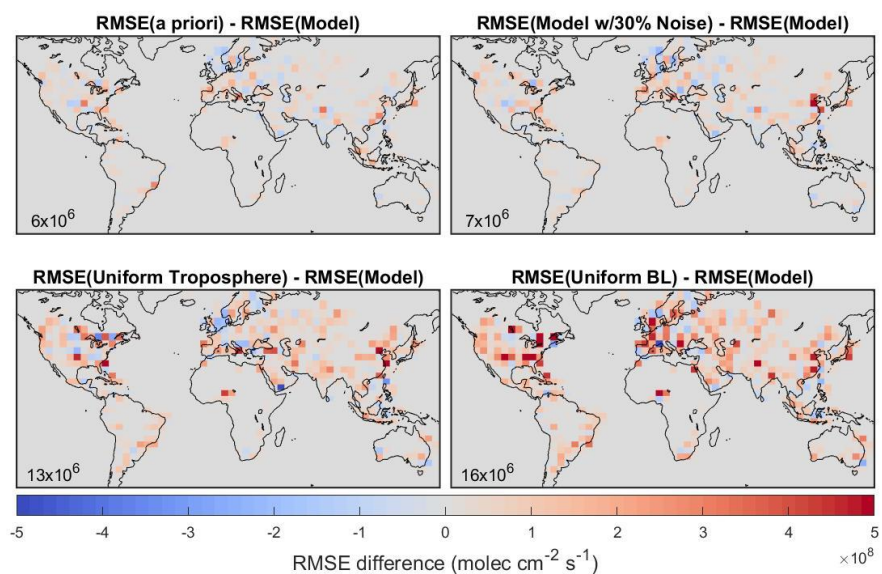
529
Figure 4: Difference between root mean square error (RMSE) of adjoint tests. Mean absolute
difference (molec/cm^2/s) values inset.
532
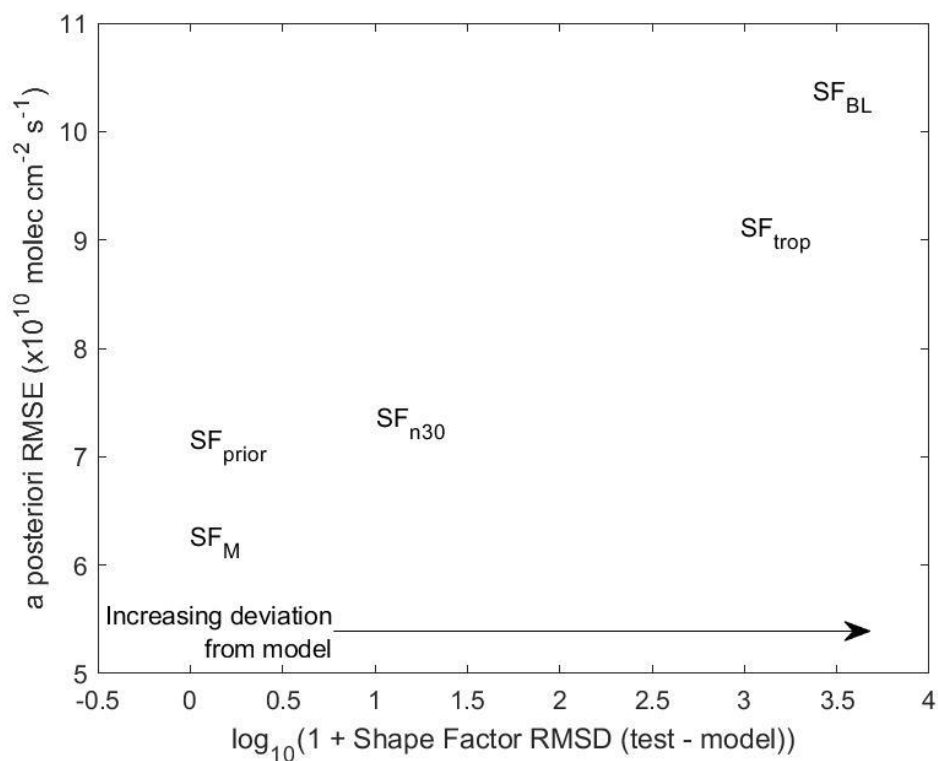
533
534 Figure 5: Scatterplot of adjoint test results. X-axis represents the deviation of the shape factor
535 from the model simulated shape factor (root mean square difference). Y-axis represents the *a*
536 *posteriori* emissions error from the adjoint inversion.
537

538

Variable	*Palmer et al., 2001*	*Eskes & Boersma, 2003*	*Boersma et al., 2016*	Notation used here
Air mass factor	AMF	M	M	M
Slant Column	Ω_S	S	N_S	Ω_s
Vertical Column	Ω_V	V	N_V	Ω_v
Scattering Weight	$w(z)$	C_l	m_l	w
Shape Factor	$S_z(z)$			$S(z)$
Averaging Kernel		A	A	A
Number density	$n(z)$	x	x_l	$n(z)$
Geometric AMF	AMF_G			M_G

539   Table 1: Lexicon comparing notation used in this paper to that used in previous studies.

540

541

Test Name	Shape Factor Source	Correlation (r) of *a posteriori* RMSE and "true" emissions	*a posteriori* RMSE ($\times 10^8$ molec/cm^2/s)		Error standard deviation ($\times 10^8$ molec/cm^2/s)		Maximum error ($\times 10^9$ molec/cm^2/s)
		if "true" emissions $> 10^{10}$ molec/cm^2/s	"true" emissions $> 10^{10}$ molec/cm^2/s	"true" emissions $> 10^{11}$ molec/cm^2/s	"true" emissions $> 10^{10}$ molec/cm^2/s	"true" emissions $> 10^{11}$ molec/cm^2/s	
SF$_M$	Model	0.03*	1.8	3.0	1.8	2.9	1.6
SF$_{prior}$	a priori	0.03*	2.0	3.2	2.0	3.3	1.6
SF$_{n30}$	Model w/ 30% noise	0.16	2.1	3.9	2.1	3.8	1.8
SF$_{trop}$	Uniform in troposphere	0.68	2.8	5.6	2.8	5.5	2.1
SF$_{BL}$	Uniform in boundary layer	0.08*	2.8	4.6	2.8	4.6	1.9

542 Table 2: Summary of error statistics for adjoint tests. Values marked * indicate that correlation is
543 not statistically significant (p>0.05)